Electrochimica Acta 504 (2024) 144949

Contents lists available at ScienceDirect

Electrochimica Acta

journal homepage: www.journals.elsevier.com/electrochimica-acta

A Cu-Zn bimetallic organic framework as protective interlayer for dendrite-free Zn deposition in zinc-based flow batteries

Pengfei Wang [a,b], Kun Zhang [c], Jing Hu [d,e,*], Menglian Zheng [a,b,c,**]

[a] State Key Laboratory of Clean Energy Utilization, Zhejiang University, Hangzhou 310027, China
[b] Institute of Thermal Science and Power Systems, School of Energy Engineering, Zhejiang University, Hangzhou 310027, China
[c] Institute of Wenzhou, Zhejiang University, Wenzhou 325036 China
[d] Department of Biological and Chemical Engineering, Aarhus University, Aarhus C 8000, Denmark
[e] Hangzhou Global Scientific and Technological Innovation Center, Zhejiang University, Hangzhou 311215, China

ARTICLE INFO

Keywords:
Flow battery
Zn dendrite
Zincophilic site
MOF
Protective interlayer

ABSTRACT

Zinc-based flow batteries hold great promise for grid-scale energy storage. However, the formation of zinc dendrites challenges their lifespan and safety. In this work, we devise a bimetallic organic framework material on carbon cloth (CuZn@MOF-CC) using a one-step dip coating method to address the dendrite issue. The prepared CuZn@MOF-CC promotes the creation of zincophilic sites on the electrode surface, facilitating smooth and uniform zinc deposition. Electrochemical csharacterizations and density functional theory (DFT) calculations reveal much stronger electronic interactions between CuZn@MOF and the zinc atoms compared to the commonly used anode material through an obvious electron interaction between the Zn atom and the Cu sites linked in the CuZn@MOF chain. By mitigating the zinc dendrite problem, this approach effectively improves the coulombic efficiency, cycle life, and safety of zinc-based flow batteries. The battery incorporating the prepared material demonstrates impressive stability, exceeding 450 cycles without dendrites at a high current density of 320 mA cm^{-2}, paving the way for efficient and reliable energy storage solutions and a sustainable future.

1. Introduction

Driven by the surge in renewable energy such as solar and wind, there is an increasing demand for efficient and cost-effective energy storage technologies [1]. Zinc-based flow batteries have gained considerable attention due to zinc's abundance, affordability, and environmental friendliness [2,3]. However, the formation of zinc dendrites during repetitive charge-discharge cycles hinders the practical implementation of zinc-based flow batteries [4]. The growth of zinc dendrites is primarily attributed to the uneven zinc deposition and the accumulation of electric field gradients, which promote localized zinc electrodeposition and dendritic growth. Researchers have made significant efforts to migrate this problem for zinc-based flow batteries [4]. Various strategies have been explored, including the addition of additives to the electrolyte (such as polyacrylamide and LiCl), [5,6] changing the physical characteristics of the battery (such as operating temperature and flow rate), [7,8] and modification of electrode materials (such as polybenzimidazole nanofiber layer and dopamine derived N-doped carbon spheres) [9,10].

Porous carbon materials can reduce local current and thus slow dendrite formation due to their three-dimensional structure and high specific surface area. However, in commonly used carbon-based electrodes such as carbon cloth and carbon felt, most of the carbon atoms are tightly bound within a hexagonal lattice of sp^2 hybridization, resulting in weak interaction between zinc and the electrode surface, leading to uneven zinc deposition. As the deposition proceeds, more zinc accumulates near the existing zinc nuclei, exacerbating the risk of zinc dendrite formation and limiting the utilization of the surface area of carbon fiber materials. Researchers have designed electrodes to achieve efficient and long-lasting operation of zinc-based flow batteries. Li et al. induced zinc deposition sites by etching N-rich defect sites on carbon fiber surfaces [11]. Tang et al. regulated the electrode interface process in zinc-based flow batteries by modulating nicotinamide [12]. Jin et al. also tried to induce zinc adsorption and deposition by introducing defect sites [13]. In addition to *in situ* etching, constructing a protective artificial interface layer on the electrode surface has become an efficient

* Corresponding author at: Department of Biological and Chemical Engineering, Aarhus University, Aarhus C 8000, Denmark.
** Corresponding author at: State Key Laboratory of Clean Energy Utilization, Zhejiang University, Hangzhou 310027, China.
E-mail addresses: jing@bce.au.dk (J. Hu), menglian_zheng@zju.edu.cn (M. Zheng).

https://doi.org/10.1016/j.electacta.2024.144949
Received 19 June 2024; Received in revised form 27 July 2024; Accepted 20 August 2024
Available online 22 August 2024

solution to achieve highly reversible zinc deposition and stripping [14]. By constructing artificial interface protective layers, it is possible to precisely control the surface properties of electrodes, preventing corrosive side reactions and regulating aspects such as surface charge density and adsorption characteristics [15–18]. For instance, the use of carbon derived from metal-organic framework/porous materials reduced the local current density on the electrode surface, [19] the interphase produced by the electrospray process inhibited side reactions such as hydrogen evolution on the electrode surface, [20] and copper nano boxes restricted the three-dimensional diffusion of zinc ions [21].

Metal-organic framework (MOF) materials represent a promising class of interface layer materials with the potential to enhance the zincophilic properties of electrodes [22,23]. The rich variety of MOF materials offers numerous options to enhance the adsorption capabilities of zinc atoms [24–27]. The adsorption potential of MOF materials relies heavily on the presence of unsaturated metal sites, which play a crucial role in their adsorption capabilities. The results showed that the addition of transition metals can provide valence electrons to better bind to the target material [28]. In the field of flow batteries, MOF materials have been the subject of some research, primarily focusing on the modification and improvement of membrane and electrode materials [29–32]. In the realm of electrodes, the application of MOFs was predominantly centered on utilizing MOF-derived carbon materials to catalyze redox reactions. There has been limited research on the deposition process [33]. To enhance these properties and achieve further optimization, the choice of metal elements becomes highly significant [34]. Among the potential choices, copper (Cu) and zinc (Zn) emerge as promising candidates for enhancing the induction effect of zinc deposition. On the one hand, the Cu and Zn atomic structures are similar, allowing them to create stable crystal structures [35,36]. On the other hand, they all have strong zincophilic properties, serving as effective zincophilic sites for inducing zinc deposition [21,37]. Although previous studies have verified the effectiveness of the MOF as a protective layer on carbon-based material for migrating zinc dendrite, it remains unclear whether and how bimetallic organic framework functions on zinc dendrite formation and the performance of zinc-based flow batteries.

This study revolutionizes the domain of zinc-based flow batteries with the innovative synthesis of a bimetallic MOF material, integrating copper and zinc. The application of this material through a one-step dip coating technique on porous electrodes represents a significant leap in addressing the persistent challenge of zinc dendrite formation. The material's design ingeniously fosters a proliferation of zincophilic sites on the electrode surface, orchestrating a uniform zinc deposition that circumvents the traditional pitfalls of electrode corrosion and side reactions. Underpinned by robust Density Functional Theory (DFT) simulations, the material's exceptional electronic synergy with zinc atoms is revealed, elucidating its superior binding energy. This insight is a testament to the material's innovative nature and its potential to redefine the standards of battery performance. The empirical validation through alkaline zinc-iron flow batteries (AZIFB) is nothing short of transformative, showcasing a quantum leap in efficiency, endurance, and safety. These enhancements are revolutionary, signaling a paradigm shift towards the broader utilization and acceptance of these batteries in grid-scale energy storage applications. This work is an innovation that propels the energy storage industry towards a horizon of sustainability and reliability, setting a new benchmark for the future of clean energy solutions.

2. Methods

2.1. Materials

The chemical reagents used in the study were all AR quality including $Na_4Fe(CN)_6$ (Macklin, Shanghai), KOH (Sinopharm, Beijing), ZnO (Macklin, Shanghai), NaOH (Sinopharm, Beijing), $C_4H_6N_2$ (Aladdin, Shanghai), CH_3OH (Sinopharm, Beijing), $Cu(NO_3)_2$ (Aladdin, Shanghai), and $Zn(NO_3)_2$ (Aladdin, Shanghai). The electrode material on the positive side was 3-mm-thick carbon felt (SGL Carbon). When installed in a flow battery, the carbon felt had a compression ratio (defined as the ratio of the thickness of the compressed felt to its original thickness) of 66 % and a thickness of 2 mm. The electrode material on the negative side was 360 μm thick carbon cloth (CC). The membrane employed was Nafion 211, manufactured by Dupont.

2.2. Preparation of CuZn@MOF carbon cloth (CuZn@MOF-CC)

CuZn@MOF nanocrystals were successfully created on a carbon cloth substrate via a dip-coating technique. To outline the standard synthesis process, a solution was initially composed by combining $Zn(NO_3)_2$ and $Cu(NO_3)_2$ in a methanolic medium and agitated to achieve a homogeneous mixture. Concurrently, a separate solution was formulated by incorporating 2-methylimidazole into methanol. These two solutions were then meticulously combined and agitated to ensure a uniform blend. A section of carbon cloth, measuring 5 cm by 5 cm, was subsequently immersed into the mixed solution and left to stand at ambient temperature, which facilitated the *in situ* synthesis of CuZn@MOF-CC. Following 24 h, the carbon cloth, now featuring the nanocrystals, was carefully removed from the reaction mixture and washed with deionized water to remove any residual reactants. Finally, the treated carbon cloth underwent vacuum drying at a temperature of 50 °C to ensure complete removal of solvent and to solidify the nanocrystal formation.

2.3. Samples characterization

The physical and structural properties of the fabricated electrodes were examined through some *ex-situ* characterization methods including the use of a scanning electron microscope (SEM, SU-8010). Additionally, energy-dispersive X-ray spectroscopy (EDS) was employed to further analyze the sample composition. To determine the makeup and crystalline arrangement of the CuZn@MOF-CC, an X-ray diffractometer (XRD, Ultimate IV) was utilized. The scanning was conducted at a pace of 2° per minute. To discern the elemental variances between the CuZn@MOF-CC and the pristine carbon cloth, X-ray photoelectron spectroscopy (XPS) and Fourier-transform infrared spectroscopy (FTIR) were deployed. The wettability of the electrode surface was assessed by measuring the contact angle of water droplets, which provided visual documentation of the measurements.

2.4. Electrochemical measurement

Electrochemical characterization was performed utilizing a VMP-3 electrochemical workstation. The setup involved a standard three-electrode system, comprising the specimen as the working electrode, and a saturated calomel electrode serving as the reference, while a platinum mesh acted as the counter electrode. The test solution environment was 0.2 mol L^{-1} of $Zn(OH)_4^{2-}$. The cyclic voltammetry (CV) assessments were executed over a potential window from −0.2 V to 1.0 V against the saturated calomel electrode (SCE), with the scanning rate varying from 10 mV s^{-1} to 100 mV s^{-1}. Furthermore, electrochemical impedance spectroscopy (EIS) was conducted, sweeping through frequencies from 200 kHz down to 50 mHz. For the zinc plating process on the CC, current densities of 5 mA cm^{-2} were applied for durations of 10 min and 30 min. After deposition, SEM was employed to capture images that provided insights into the morphology of the zinc deposits on the CC surface.

2.5. Battery test

A flow battery was assembled to test electrode performance. The CuZn@MOF-CC composite material was deployed as the negative side. The active reaction surface measured 5 cm*5 cm. The current collection

was facilitated by two graphite plates designed with a serpentine flow field. The negative electrolyte consisted of 60 mL of 0.4 mol L^{-1} Zn $(OH)_4^{2-}$ + 3.8 mol L^{-1} OH^-, while the positive electrolyte comprised 60 mL 0.8 mol L^{-1} $Fe(CN)_6^{4-}$ + 3 mol L^{-1} OH^-. The battery was charged and discharged on the charge and discharge tester (CT-4008Tn, Neware). The rate performance and long cycle performance of the battery were tested at different current densities. The charge capacity was managed by regulating the duration of the charging phase, and the discharge was ceased once the voltage dropped to 0.1 V. According to the flow rate calculation method reported in the literature [38], the flow rate was 35 ml min^{-1} when the current density was 80 mA cm^{-2}. As the current density increased, the flow rate increased proportionally. To observe the deposition of zinc on the electrode surface, the CC of the anode is removed at the end of the charging phase. SEM was used to photograph the appearance of zinc deposition on the surface of CC.

2.6. Computation details

First-principles calculations rooted in DFT were executed utilizing the Vienna Ab initio Simulation Package (VASP) [39,40]. The calculations incorporated the projector-augmented wave (PAW) approach and the Perdew-Burke-Ernzerhof (PBE) functional within the framework of the generalized gradient approximation (GGA) to model electron exchange and correlation [41]. A plane-wave basis set with a cut-off energy of 500 eV was established for the simulations. The Brillouin zone integration was conducted using a k-point grid; a 1 × 1 × 1 grid was applied for the CuZn@MOF structure, while a 2 × 1 × 1 grid was used for the carbon cloth structure. Structural optimizations were performed using the conjugate gradient technique, with convergence thresholds set for energy at 10^{-5} eV and for force at 0.02 eV/Å. The adsorption energy of Zn on the substrate was quantified using the formula:

$$E_{ads} = E_{mol/surf} - E_{surf} - E_{mol} \quad (1)$$

where $E_{mol/surf}$, E_{surf}, and E_{mol} are the energies of the system consisting of adsorbate molecules on the surface, the energy of a clean surface, and the energy of isolated molecules in a cubic periodic box, respectively. The data were treated with the assistance of vaspkit software 1.4.0 [42].

3. Results and discussion

In this work, carbon cloth was chosen as the substrate for the synthetic material. The nanoparticles can be uniformly loaded on the fiber

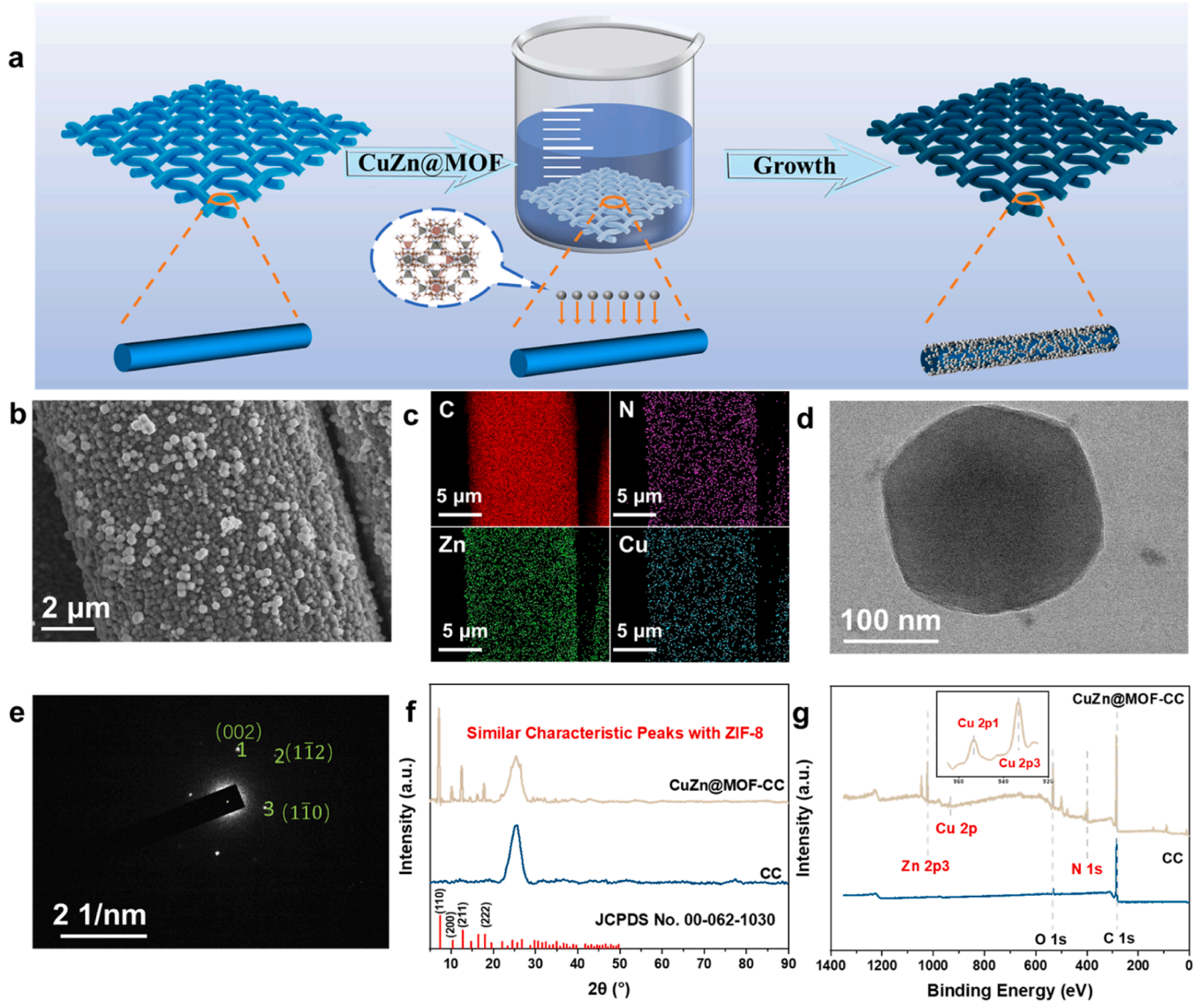

Fig. 1. (a) Synthesis process of CuZn@MOF-CC. (b) SEM images of CuZn@MOF-CC. (c) EDS mapping of CuZn@MOF-CC. (d) TEM images of CuZn@MOF crystal. (e) Electron diffraction pattern of CuZn@MOF crystal. (f) XRD patterns of CC and CuZn@MOF-CC. (g) XPS survey of CC and CuZn@MOF-CC.

surface because of the regular arrangement of fibers in carbon cloth compared with carbon felt. As shown in Fig. 1a, carbon cloth was soaked in CuZn@MOF solution by using the dip coating method so that CuZn@MOF nanocrystals *in situ* grow uniformly on the fiber surface. Scanning electron microscopy (SEM) was employed to capture the morphology of the fiber surface to better understand the coverage of crystal particles on the surface of carbon fibers. The original carbon fiber surface appeared relatively clean with minor grooves. Following coating, as shown in Fig. 1b and Fig. S1, CuZn@MOF crystals uniformly covered the fiber surface with a long-range ordered array structure. *In situ*-grown CuZn@MOF particles exhibited a distinct crystal structure on the carbon fiber surface. The crystals displayed a uniform size of about 100–200 nm, regular morphology, and a well-defined dodecahedral shape. As shown in Fig. 1c, energy-dispersive X-ray spectroscopy (EDS) confirmed the presence of Cu and Zn elements, validating the introduction of bimetallic materials. The ratio of Zn to Cu was about 20:1. The mapping distribution of Cu, Zn, and N elements was consistent, confirming the successful doping of CuZn@MOF crystals. In this case, the N element originated from the ligand 2-methylimidazole. Transmission electron microscope (TEM) images showed that CuZn@MOF crystals were regular dodecahedrons with side lengths of about 100 nm (Fig. 1d and Fig. S2). Points 1 and 3 correspond to the (002) and (110) crystal plane family of the ZIF-8 structure, respectively in the electron diffraction pattern of CuZn@MOF crystal (Fig. 1e). The ZIF-8-like structure could be determined. The calculated crystal band axis was [110]. X-ray diffractometer (XRD) results also showed that CuZn@MOF crystals and ZIF-8 had similar crystal structures (Fig. 1f). In addition to the characteristic peaks of C from the (002) crystal face of CC, the strong peaks of CuZn@MOF-CC at $2\theta = 7.30^\circ$, 10.35°, 12.70°, and 18.00° corresponded to the plane (110), (200), (211) and (222), respectively, indicating that the prepared CuZn@MOF has a high crystallinity.

The composition and structure of the prepared materials were further confirmed. As shown in Fig. 1g, obvious peaks of Cu, Zn, and N elements were detected for CuZn@MOF-CC through X-ray photoelectron spectroscopy (XPS). The sub-peak fitting results of CuZn@MOF-CC are shown in Fig. S3. The three fitting peaks at 399.28 eV, 400.69 eV, and 406.95 eV in the spectrum of N 1 s were attributed to N-C, N and Cu or Zn coordination bonds in imidazole and N=C bonds, respectively. In the spectrum of Cu 2p, two peaks at 953.85 eV and 934.10 eV belonged to Cu 2p1/2 and Cu 2p3/2. The other two satellite peaks belonged to Cu^{+}. Fourier infrared spectroscopy also confirmed the successful growth of CuZn@MOF on the fiber surface (Fig. S4).

Different electrode materials were assessed by measuring their contact angles to determine their hydrophilic properties. Fig. S5 illustrates the contact angles using the sessile drop method. Due to the relatively hydrophobic surface characteristics of carbon cloth, droplets on its surface formed a contact angle of 136.4° and maintained this configuration for an extended period. Droplets on the surface of CuZn@MOF-CC exhibited a smaller contact angle and were rapidly absorbed, confirming a substantial improvement in its hydrophilicity. The enhanced hydrophilicity promoted the rapid transport of zincate ions on the electrode surface. This not only reduced concentration polarization of the battery, enhancing overall efficiency but also accelerated and evened out the zinc deposition process. Preventing zincate ions scarcity on the electrode surface, helped mitigate tip aggregation, ultimately inhibiting the formation of zinc dendrites.

Electrochemical tests were performed in a three-electrode test system. Tafel tests were performed to measure the undesired hydrogen evolution reaction (HER) and corrosion characteristics of the material surface (Fig. 2a). As expected, CuZn@MOF-CC (−0.17 V) had a higher

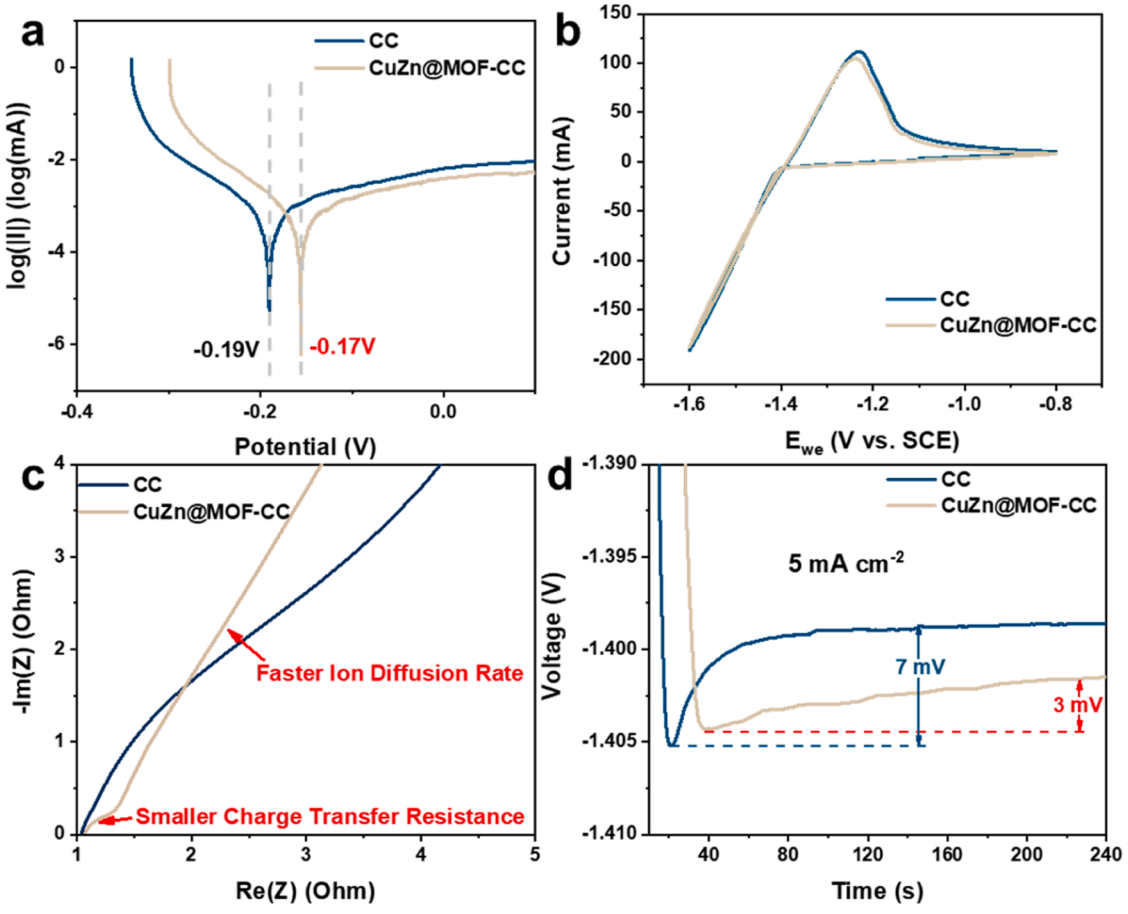

Fig. 2. (a) Tafel corrosion potential, (b) CV tests, (c) EIS results and (d) Zinc nucleation overpotential at 5 mA cm^{-2} of CC and CuZn@MOF-CC.

corrosion potential than CC (−0.19 V) and smaller corrosion current. The CuZn@MOF layer increased electrode stability and prevented corrosion or passivation on its surface. Strong hydrogen evolution corrosion was more difficult to occur on the surface of CuZn@MOF-CC. This allowed the electrode to maintain high stability and a long cycle life during the long-term cycle. Cyclic voltammetry (CV) was used to measure the electrochemical activity of the redox couple ($Zn/Zn(OH)^-$) (Fig. 2b). The CV curve of CuZn@MOF-CC basically coincided with that of CC, which proved that the introduction of CuZn@MOF had no significant negative effect on its electrochemical activity. Electrochemical impedance spectroscopy (EIS) results also showed that CuZn@MOF-CC had smaller semicircular diameters in the high-frequency region, which meant a smaller charge transfer resistance R_{ct} (Fig. 2c). This result proved that the electrical conductivity of the electrode surface was improved, resulting in a faster charge transfer rate. This acceleration in charge transfer contributed to a more uniform distribution of charge, thereby promoting uniform zinc deposition. Zinc nucleation overpotential was measured to detect the effect of CuZn@MOF doping on zinc deposition (Fig. 2d). Compared with CC (7 mV), CuZn@MOF-CC (3 mV) exhibited a reduction in the nucleation overpotential of zinc. This indicated that during the nucleation stage of zinc deposition, CuZn@MOF-CC experienced less difficulty in nucleation, leading to more intensive and rapid nucleation. Consequently, zinc deposition on the electrode surface became more uniform and smoother compared to that with CC.

To examine the inhibition effect of the CuZn@MOF-CC on zinc dendrites, zinc was electrochemically deposited onto different substrates, followed by observing the deposition morphology of zinc. Electrodeposition was conducted separately on each material, employing a current of 5 mA cm^{-2} for durations of 10 and 30 min (Fig. 3), respectively. Following the 10 min electrodeposition, zinc deposition on the CC surface exhibited a disorderly and uneven pattern (Fig. 3b, d). Notably, sizable zinc clusters formed amidst the fibers, reminiscent of thorns. Most of the fiber surfaces remained uncovered by zinc, with only isolated regions accumulating a significant quantity of zinc. The zinc deposition displayed sharp protrusions on both the fiber surface and the inter-fiber regions. When electrochemical deposition continued for 30 min, zinc coverage on CC fiber surfaces exhibited a slight increase, yet numerous areas remained uncovered. The phenomenon of zinc clustering became more conspicuous, with zinc clusters surpassing the fiber diameter. In some regions, a significant amount of zinc has accumulated between the fibers, completely covering the carbon fibers. In contrast, zinc deposition on CuZn@MOF-CC exhibited a more uniform distribution (Fig. 3e–h). The fibers were essentially enveloped by the deposited zinc, and there was a notable absence of zinc clustering between the fibers, demonstrating the excellent reversibility of CuZn@MOF-CC. On the surface of CuZn@MOF, the morphology of zinc deposition had not changed significantly with time. The zinc deposition appeared much smoother, with only a few slender wrinkled patterns on the fiber surface. There were no noticeable irregular protrusions on the fiber surface. Atomic force microscopy (AFM) was also used to photograph the surface morphology of CuZn@MOF-CC after zinc deposition. The three-dimensional image is shown in Fig. S6. It is evident that, in comparison to CC, CuZn@MOF-CC demonstrated substantial enhancements in both the uniformity and morphology of zinc deposition.

The surface nucleation of untreated CC is difficult and the nucleation process of zinc is uneven. As the deposition process continues, zinc tends to continue to deposit at nucleated sites, gradually forming bulges or even dendrites. On the surface of CuZn@MOF-CC, the nucleation overpotential is significantly reduced due to the stronger zincophile. Additionally, more sites can be used for zinc nucleation, avoiding the accumulation of zinc deposits in some areas. With the growth of time, a flat and uniform zinc layer is formed on the surface of the fiber (Fig. 4a).

To explain the deposition characteristics of Zn atoms on the surface of CuZn@MOF, DFT calculations were performed. In order to explain the effects of CuZn@MOF on the Zn atom adsorption process, we first explored the electronic structure of CC (simplified to a single layer of graphene, GRA) and CuZn@MOF (Fig. S7) with adsorbed Zn atoms. Fig. 4b and c present the charge density difference of GRA and CuZn@MOF, respectively, with Zn atom adsorption from a three-dimensional view. For GRA, it could be seen that the depletion of electron density appeared on the hollow site of the six-membered rings and the electron density accumulation occurred on the Zn atom, indicating a charge transfer happens from the hollow site of the six-membered rings to the Zn atom. However, unlike GRA, the CuZn@MOF had one additional feature: an obvious electron interaction between the Zn atom and the Cu sites linked in the CuZn@MOF chain. The depletion of electron density appeared between its Cu site and the hollow site of the imidazolium rings in the CuZn@MOF chain, which would result in changes for more effective binding strength of the Zn atom adsorbed. In addition, the structural similarity of ZIF-8 to CuZn@MOF material is considered. Fig. S7b and S7c presented the charge density difference of ZIF-8 and CuZn@MOF with Zn atom adsorption from a three-dimensional view, respectively. For ZIF-8, it could be seen that the depletion of electron density appeared on the hollow site of the imidazolium rings, and the electron density accumulation occurred on the Zn atom, indicating a charge transfer happened from the on the hollow site of the imidazolium rings to Zn atom. In comparison, there was no obvious electron interaction between the Zn atom and the Zn sites linked in the ZIF-8 chain. However, unlike ZIF-8, the CuZn@MOF had one additional feature: an obvious electron interaction between the Zn atom and the Cu sites linked in the CuZn chain. The depletion of electron density appeared between

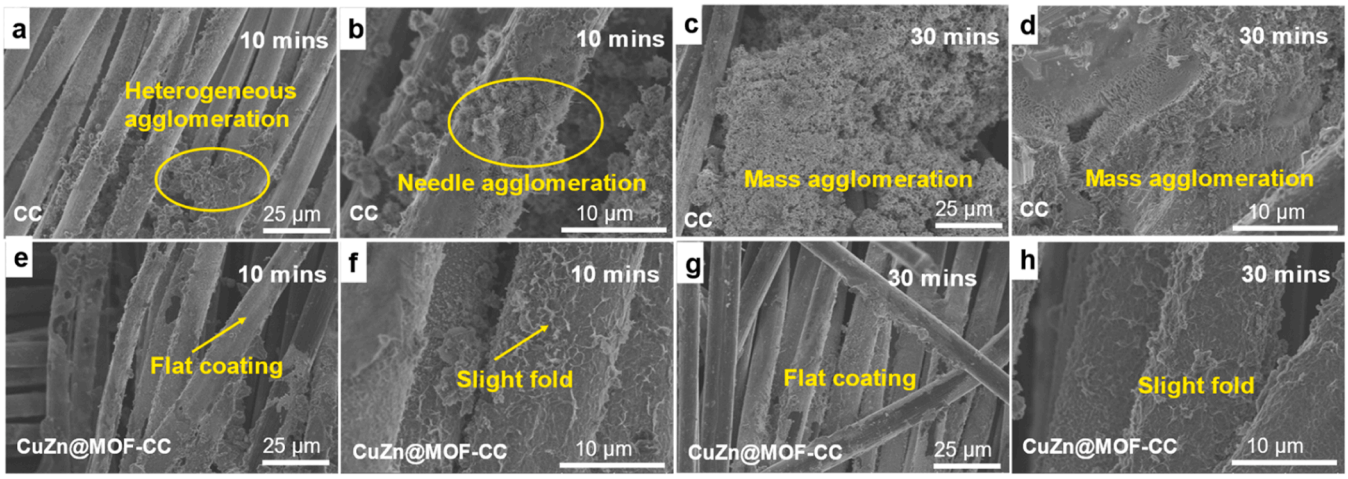

Fig. 3. SEM images of zinc deposition on the surface of CC, and CuZn@MOF-CC at different deposition time.

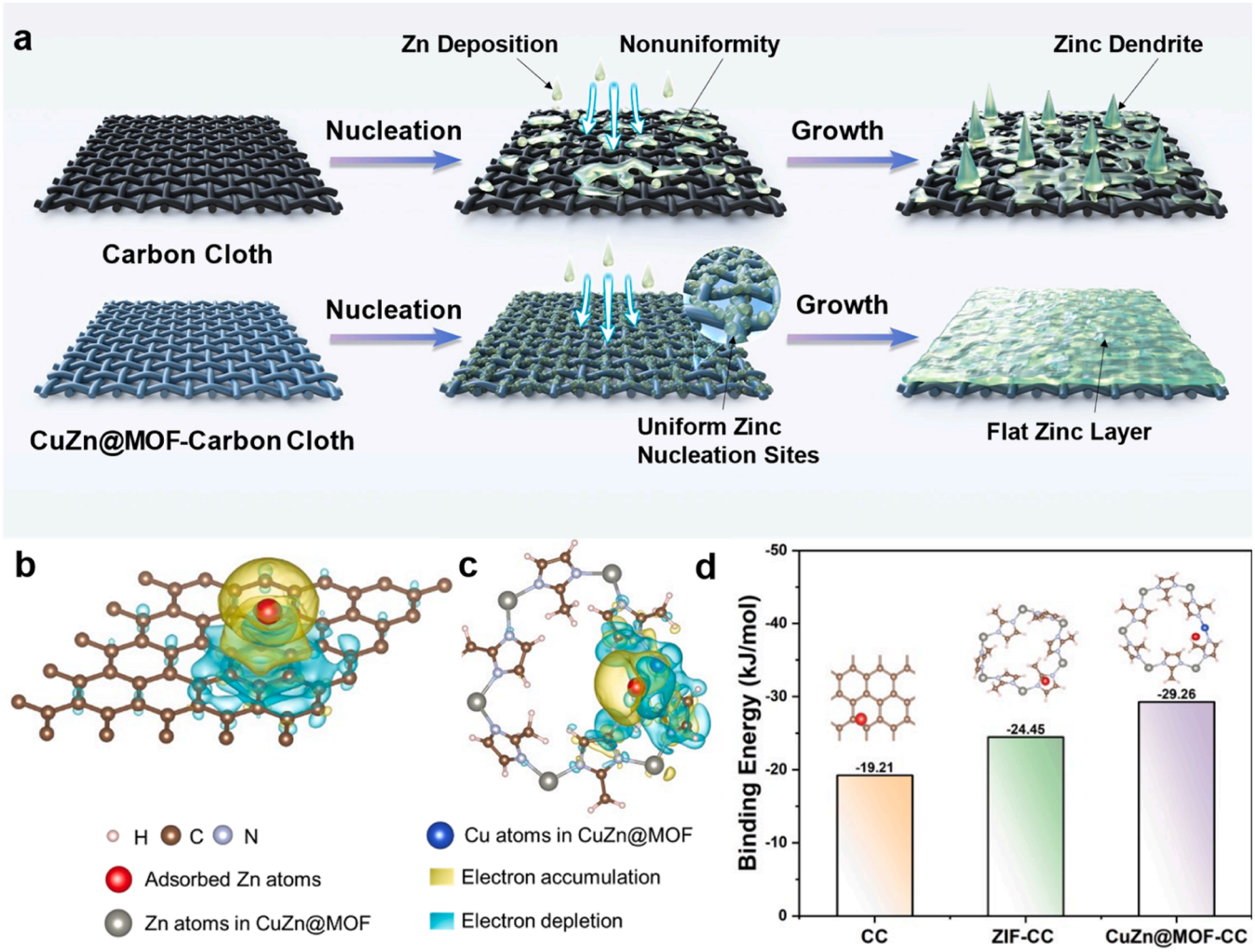

Fig. 4. a) Nucleation and deposition of zinc on surfaces of CC and CuZn@MOF-CC. b,c) Interfacial charge-density models of CC and CuZn@MOF with Zn atom adsorption. d) Calculated binding energy of Zn atom with CC, ZIF-8 and CuZn@MOF.

its Cu site and the hollow site of the imidazolium rings in the CuZn@-MOF chain, which would result in changes for more effective binding strength of the Zn atom adsorbed. Then, we performed the first-principles calculation for the adsorption energies of the Zn atom on CC, ZIF-8 and CuZn@MOF (Fig. 4d). Compared with CC(−19.21 kJ mol^{-1}) and ZIF-8 (−24.45 kJ mol^{-1}), CuZn@MOF had a stronger interaction with the Zn atom (−29.26 kJ mol^{-1}). The calculation results confirmed that CuZn@MOF was suitable as the zincophilic site, and Zn atoms deposited on CuZn@MOF had a low nucleation barrier and uniform deposition effect.

An AZIFB with a serpentine flow channel was assembled and subjected to charge-discharge cycling tests to evaluate the performance and stability of CuZn@MOF-CC in batteries. Nafion 211 was utilized as the membrane, CuZn@MOF-CC was employed as the anode in the battery, and CC was used as the contrast and underwent the same testing on the anode. The rate performance of the AZIFB was examined at various current densities. The voltage efficiency (VE) of the battery at current densities ranging from 80 mA cm^{-2} to 320 mA cm^{-2} was plotted in Fig. 5a. CuZn@MOF-CC resulted in an approximately 3 % improvement in the VE of the AZIFB, indicating reduced voltage loss during the charge-discharge process. It could be attributed to the lower charging voltage, as shown in Fig. 5b. Due to the lower nucleation overpotential during zinc deposition, the AZIFB with CuZn@MOF-CC exhibited lower charging voltage compared to the AZIFB with CC. Another reason for the decrease in the polarization loss was the enhanced mass transfer due to the improvement of wettability. This also implied that the AZIFB with CuZn@MOF-CC could achieve a higher capacity at the same cut-off voltage. To further verify the effect of bimetallic MOF on the performance of the battery, the coulombic efficiency (CE) after the first 100 cycles of the flow battery with different electrodes was calculated (Fig. 5c). The cell with CuZn@MOF-CC showed the highest CE (97.1 %), which can be attributed to the improvement of the uniformity of zinc deposition and the inhibition of corrosion caused by side reactions. In the long cycle, black zinc particles appeared in the negative electrode tank (Fig. S8), which was the accumulation of “dead zinc” on the electrode surface carried out by the electrolyte flow. This also had a certain impact on the CE of the battery. The AZIFBs with CuZn@MOF-CC underwent long-term cycling at a current density of 80 mA cm^{-2} for 275 h without significant voltage spikes or efficiency decay (Fig. 5d) and maintained stable CE, VE and energy efficiency (EE) in the long cycle (Fig. 5e). The AZIFB with CC had a sharp voltage increase after only 120 h, which was caused by excessive polarization, and the efficiency of the battery also dropped rapidly. The long lifetime demonstrated the excellent cycling stability of the AZIFB with CuZn@MOF-CC. There were slight fluctuations in the efficiency curve of the battery. The observed fluctuation in the battery efficiency showed a significant cyclical change, and the period is approximately 24 h. Therefore, it is speculated that this cyclical fluctuation was probably associated with the temperature variations throughout the day. At a current density of 320 mA cm^{-2}, the AZIFB with CC exhibited noticeable short-circuiting

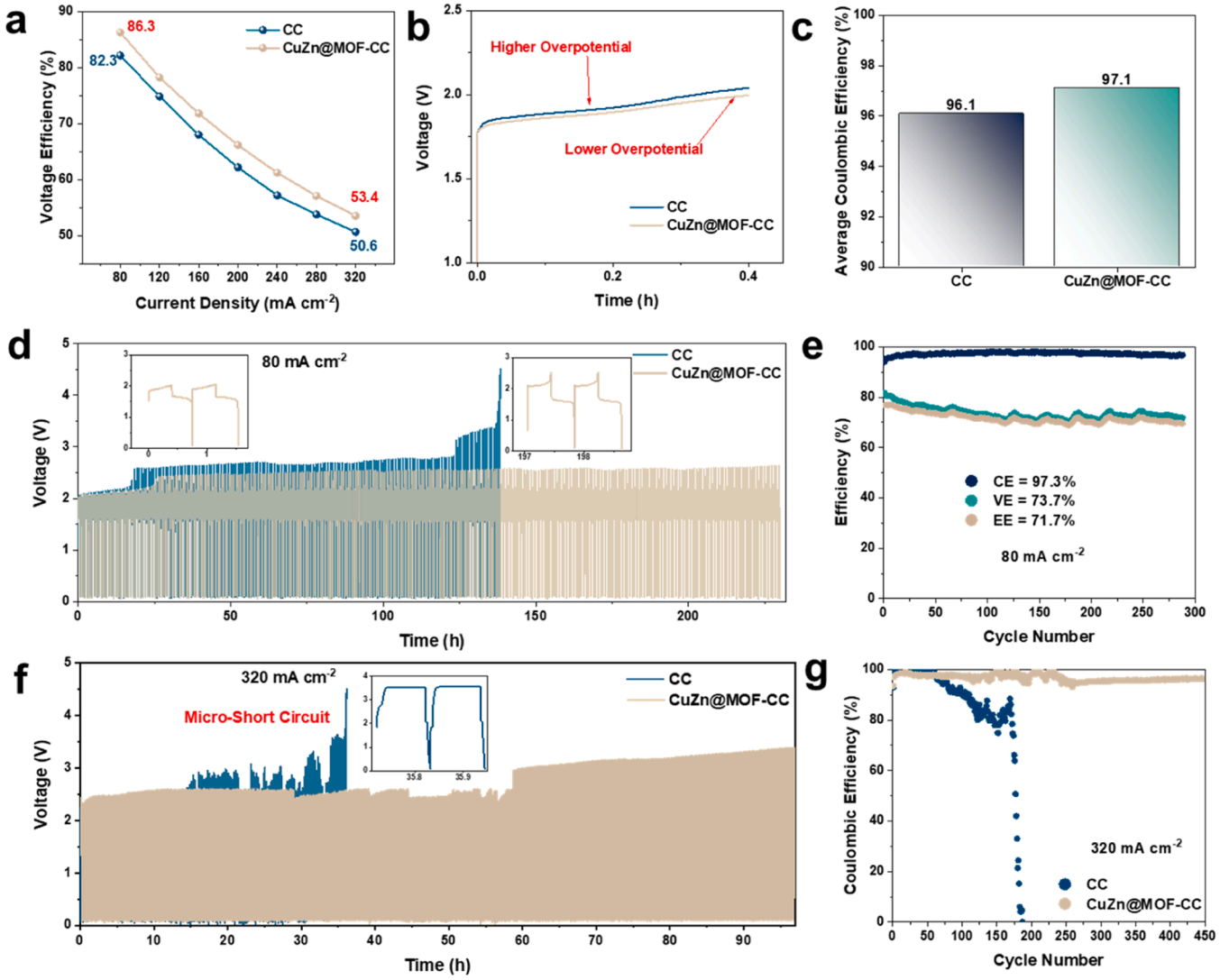

Fig. 5. (a) VE of AZIFB with CC and CuZn@MOF-CC negative electrode at different current densities. (b) Voltage-time curves of AZIFB with CC and CuZn@MOF-CC at 80 mA cm^{-2}. (c) Average CE over a hundred cycles of AZIFB with different electrodes. (d) Voltage-time curves of AZIFB with CC and CuZn@MOF-CC at 80 mA cm^{-2}. (e) CE, VE, and EE of AZIFB with CC and CuZn@MOF-CC at 80 mA cm^{-2}. (f) Voltage-time curves of AZIFB with CC and CuZn@MOF-CC at 320 mA cm^{-2}. (g) CE of AZIFB with CC and CuZn@MOF-CC at 320 mA cm^{-2}.

phenomena after only 180 cycles (Fig. 5f). It could be attributed to the growth of zinc dendrites on the negative electrode. Meanwhile, the AZIFB with CuZn@MOF-CC could still maintain stable performance during 450 cycles (Fig. 5f and 5g). The improvement in the uniformity of zinc deposition with CuZn@MOF-CC was confirmed. The negative electrodes were extracted at the end of the charging, and SEM (Fig. S9) was employed to examine the morphology of zinc deposition on the negative electrode. It was obvious that zinc deposition in AZIFB with CuZn@MOF-CC was more uniform and flatter at high current density. The zinc in AZIFB with CC had irregular clumping and protruding. All the battery test results have confirmed that CuZn@MOF-CC can improve the performance of the zinc-based flow battery, which is expected to facilitate the large-scale application of dendrite-free zinc-based flow batteries.

4. Conclusions

In our study, we introduced a novel electrode interface material that stood to revolutionize zinc-based flow batteries. By pioneering the deposition of a bimetallic organic framework of copper and zinc (CuZn@MOF) onto a carbon cloth electrode, we have not only enhanced the formation of zinc nucleation sites on the electrode surface but also mitigated hydrogen evolution, leading to improved morphology and uniformity of zinc deposition. This advancement has significantly extended the cycle life of the batteries, with stable operation achievable for up to 275 h in laboratory conditions and an impressive cycle count of 450 even at high current densities of 320 mA cm^{-2}. The novel material's porous structure, rich in zincophilic sites, effectively impeded the growth of zinc dendrites, thereby enhancing battery performance. Supported by DFT calculations that revealed a strong electron interaction between Zn atoms and CuZn@MOF, resulting in a higher binding energy, our innovation underscored the material's stability and performance. By integrating this new electrode material into the negative electrode of zinc-based flow batteries, we have significantly improved CE and prolonged the cycle life. Addressing the critical challenge of zinc dendrite formation, our work offers a pathway to enhance the stability, cycle life, and safety of these batteries, laying a solid foundation for their widespread adoption in grid-scale energy storage applications and heralding a new era in sustainable energy solutions.

CRediT authorship contribution statement

Pengfei Wang: Writing – original draft, Validation, Methodology, Investigation, Data curation. **Kun Zhang:** Writing – original draft, Software. **Jing Hu:** Writing – review & editing, Funding acquisition, Conceptualization. **Menglian Zheng:** Writing – review & editing, Funding acquisition, Conceptualization.

Declaration of competing interest

The authors declare that they have no known competing financial interests or personal relationships that could have appeared to influence the work reported in this paper.

Data availability

Data will be made available on request.

Acknowledgments

The authors greatly acknowledge the financial support from National Natural Science Foundation of China (No. 22208287, No. 51606164), the Fundamental Research Funds for the Central Universities (No. 2022ZFJH004), and the China Postdoctoral Science Foundation (No. 2022M712736).

Supplementary materials

Supplementary material associated with this article can be found, in the online version, at doi:10.1016/j.electacta.2024.144949.

References

[1] N.A. Sepulveda, J.D. Jenkins, A. Edington, D.S. Mallapragada, R.K. Lester, The design space for long-duration energy storage in decarbonized power systems, Nat. Energy 6 (2021) 506–516, https://doi.org/10.1038/s41560-021-00796-8.
[2] Z. Yuan, Y. Yin, C. Xie, H. Zhang, Y. Yao, X. Li, Advanced Materials for Zinc-based flow battery: development and challenge, Adv. Mater. 31 (2019) 1902025, https://doi.org/10.1002/adma.201902025.
[3] P. Wang, K. Zhang, H. Li, J. Hu, M. Zheng, Enhanced ion transport through mesopores engineered with additional adsorption of layered double hydroxides array in alkaline flow batteries, Small (2023) 2308791, https://doi.org/10.1002/smll.202308791.
[4] Y. Zuo, K. Wang, P. Pei, M. Wei, X. Liu, Y. Xiao, P. Zhang, Zinc dendrite growth and inhibition strategies, Mater. Today Energy 20 (2021) 100692, https://doi.org/10.1016/j.mtener.2021.100692.
[5] X. Guo, Z. Zhang, J. Li, N. Luo, G.L. Chai, T.S. Miller, F. Lai, P. Shearing, D.J. L. Brett, D. Han, Z. Weng, G. He, I.P. Parkin, Alleviation of dendrite formation on zinc anodes via electrolyte additives, ACS Energy Lett. 6 (2021) 395–403, https://doi.org/10.1021/acsenergylett.0c02371.
[6] Q. Zhang, J. Luan, L. Fu, S. Wu, Y. Tang, X. Ji, H. Wang, The three-dimensional dendrite-free zinc anode on a copper mesh with a zinc-oriented polyacrylamide electrolyte additive, Angew. Chem. Int. Ed. 58 (2019) 15841–15847, https://doi.org/10.1002/anie.201907830.
[7] J. Hu, M. Yue, H. Zhang, Z. Yuan, X. Li, A boron nitride nanosheets composite membrane for a long-life zinc-based flow battery, Angew. Chem. Int. Ed. 59 (2020) 6715–6719, https://doi.org/10.1002/anie.201914819.
[8] K. Wang, Y. Xiao, P. Pei, X. Liu, Y. Wang, A phase-field model of dendrite growth of electrodeposited zinc, J. Electrochem. Soc. 166 (2019) D389–D394, https://doi.org/10.1149/2.0541910jes.
[9] Q. Jian, Y. Wan, J. Sun, M. Wu, T. Zhao, A dendrite-free zinc anode for rechargeable aqueous batteries, J. Mater. Chem. A 8 (2020) 20175–20184, https://doi.org/10.1039/D0TA07348B.
[10] F. Zhang, T. Liao, C. Liu, H. Peng, W. Luo, H. Yang, C. Yan, Z. Sun, Biomineralization-inspired dendrite-free Zn-electrode for long-term stable aqueous Zn-ion battery, Nano Energy 103 (2022) 107830, https://doi.org/10.1016/j.nanoen.2022.107830.
[11] W. Lu, P. Xu, S. Shao, T. Li, H. Zhang, X. Li, Multifunctional carbon felt electrode with N-rich defects enables a long-cycle zinc-bromine flow battery with ultrahigh power density, Adv. Funct. Mater. 31 (2021) 2102913, https://doi.org/10.1002/adfm.202102913.
[12] J. Yang, H. Yan, H. Hao, Y. Song, Y. Li, Q. Liu, A. Tang, Synergetic modulation on solvation structure and electrode interface enables a highly reversible zinc anode for zinc–iron flow batteries, ACS Energy Lett. 7 (2022) 2331–2339, https://doi.org/10.1021/acsenergylett.2c00560.
[13] J.H. Lee, R. Kim, S. Kim, J. Heo, H. Kwon, J.H. Yang, H.T. Kim, Dendrite-free Zn electrodeposition triggered by interatomic orbital hybridization of Zn and single vacancy carbon defects for aqueous Zn-based flow batteries, Energy Environ. Sci. 13 (2020) 2839–2848, https://doi.org/10.1039/D0EE00723D.
[14] M. He, C. Shu, A. Hu, R. Zheng, M. Li, Z. Ran, J. Long, Suppressing dendrite growth and side reactions on Zn metal anode via guiding interfacial anion/cation/H2O distribution by artificial multi-functional interface layer, Energy Storage Mater. 44 (2022) 452–460, https://doi.org/10.1016/j.ensm.2021.11.010.
[15] H. Wang, Q. Li, S. Huang, L. Zhou, L. Mei, Z. Wu, B. Qu, W. Wei, X. Ji, Y. Chen, L. Chen, Controlled deposition via a bifunctional layer enables dendrite-free zinc metal batteries, Chem. Eng. J. 470 (2023) 144147, https://doi.org/10.1016/j.cej.2023.144147.
[16] W. Deng, N. Zhang, X. Wang, Hybrid interlayer enables dendrite-free and deposition-modulated zinc anodes, Chem. Eng. J. 432 (2022) 134378, https://doi.org/10.1016/j.cej.2021.134378.
[17] L. Zhi, C. Liao, P. Xu, F. Sun, C. Yuan, F. Fan, G. Li, Z. Yuan, X. Li, An artificial bridge between the anode and the anolyte enabled by an organic ligand for sustainable zinc-based flow batteries, Energy Environ. Sci. 17 (2024) 717–726, https://doi.org/10.1039/D3EE02693K.
[18] M. Na, V. Singh, R.H. Choi, B.G. Kim, H.R. Byon, Zn glutarate protective layers *in situ* form on Zn anodes for Zn redox flow batteries, Energy Storage Mater. 57 (2023) 195–204, https://doi.org/10.1016/j.ensm.2023.02.010.
[19] Z. Wang, J. Huang, Z. Guo, X. Dong, Y. Liu, Y. Wang, Y. Xia, A metal-organic framework host for highly reversible dendrite-free zinc metal anodes, Joule 3 (2019) 1289–1300, https://doi.org/10.1016/j.joule.2019.02.012.
[20] S. Jin, Y. Shao, X. Gao, P. Chen, J. Zheng, S. Hong, J. Yin, Y.L. Joo, L.A. Archer, Designing interphases for practical aqueous zinc flow batteries with high power density and high areal capacity, Sci. Adv. 8 (2022) eabq4456, https://doi.org/10.1126/sciadv.abq4456.
[21] Y. Zeng, P.X. Sun, Z. Pei, Q. Jin, X. Zhang, L. Yu, X. W, David) Lou, Nitrogen-doped carbon fibers embedded with zincophilic Cu nanoboxes for stable Zn-metal anodes, Adv. Mater. 34 (2022) 2200342, https://doi.org/10.1002/adma.202200342.
[22] P. Wu, Y. Cao, H. Cao, Y. Liu, X. Huang, J. Zhang, Y. Cao, Y. Long, Y. Zhai, Z. Wu, Q. Zheng, D. Lin, An *in-situ* grown high-efficiency Zn-terephthalate metal–organic framework/ZnO hybrid interface protection layer to achieve highly reversible dendrite-free Zn anodes, Chem. Eng. J. 474 (2023) 145955, https://doi.org/10.1016/j.cej.2023.145955.
[23] M. Liu, L. Yang, H. Liu, A. Amine, Q. Zhao, Y. Song, J. Yang, K. Wang, F. Pan, Artificial solid-electrolyte interface facilitating dendrite-free zinc metal anodes via nanowetting effect, ACS Appl. Mater. Interfaces 11 (2019) 32046–32051, https://doi.org/10.1021/acsami.9b11243.
[24] X. Zeng, J. Zhao, Z. Wan, W. Jiang, M. Ling, L. Yan, C. Liang, Controllably electrodepositing ZIF-8 protective layer for highly reversible zinc anode with ultralong lifespan, J. Phys. Chem. Lett. 12 (2021) 9055–9059, https://doi.org/10.1021/acs.jpclett.1c01834.
[25] L. Lei, Y. Zheng, X. Zhang, Y. Su, X. Zhou, S. Wu, J. Shen, A ZIF-8 host for dendrite-free zinc anodes and N,O dual-doped carbon cathodes for high-performance zinc-ion hybrid capacitors, Chem. Asian J. 16 (2021) 2146–2153, https://doi.org/10.1002/asia.202100526.
[26] X. Liu, F. Yang, W. Xu, Y. Zeng, J. He, X. Lu, Zeolitic Imidazolate Frameworks as Zn^{2+} modulation layers to enable dendrite-free Zn anodes, Adv. Sci. 7 (2020) 2002173, https://doi.org/10.1002/advs.202002173.
[27] Y. Long, X. Huang, Y. Li, M. Yi, J. Hou, X. Zhou, Q. Hu, Q. Zheng, D. Lin, *In-situ* regulation of zinc metal surface for dendrite-free zinc-ion hybrid supercapacitors, J. Colloid Interface Sci. 614 (2022) 205–213, https://doi.org/10.1016/j.jcis.2022.01.072.
[28] A.M. Ebrahim, T.J. Bandosz, Ce(III) doped Zr-based MOFs as excellent NO_2 adsorbents at ambient conditions, ACS Appl. Mater. Interfaces 5 (2013) 10565–10573, https://doi.org/10.1021/am402305u.
[29] J. Yuan, C. Zhang, Q. Qiu, Z.Z. Pan, L. Fan, Y. Zhao, Y. Li, Highly selective metal-organic framework-based (MOF-5) separator for non-aqueous redox flow battery, Chem. Eng. J. 433 (2022) 133564, https://doi.org/10.1016/j.cej.2021.133564.
[30] P. Sharma, R. Goswami, S. Neogi, V.K. Shahi, Devising ultra-robust mixed-matrix membrane separators using functionalized MOF–poly(phenylene oxide) for high-performance vanadium redox flow batteries, J. Mater. Chem. A 10 (2022) 11150–11162, https://doi.org/10.1039/D1TA10715A.
[31] S. Peng, L. Zhang, C. Zhang, Y. Ding, X. Guo, G. He, G. Yu, Gradient-distributed metal–organic framework–based porous membranes for nonaqueous redox flow batteries, Adv. Energy Mater. 8 (2018) 1802533, https://doi.org/10.1002/aenm.201802533.
[32] X. Zhang, D. Zhang, L. Liu, K. Zhang, Y. Zhang, J. Zhao, L. Han, M. Jing, J. Liu, C. Yan, MOF-derived W/Zr bimetallic oxides@Carbon for comprehensively remedying melamine foam electrode defects in vanadium redox flow batteries, Chem. Eng. J. 467 (2023) 143360, https://doi.org/10.1016/j.cej.2023.143360.
[33] Y. Li, L. Ma, Z. Yi, Y. Zhao, J. Mao, S. Yang, W. Ruan, D. Xiao, N. Mubarak, J. Wu, T.S. Zhao, Q. Chen, J.K. Kim, Metal–organic framework-derived carbon as a positive electrode for high-performance vanadium redox flow batteries, J. Mater. Chem. A 9 (2021) 5648–5656, https://doi.org/10.1039/D0TA10580E.
[34] Y. Jin, J. Wu, J. Wang, Y. Fan, S. Zhang, N. Ma, W. Dai, Highly efficient capture of benzothiophene with a novel water-resistant-bimetallic Cu-ZIF-8 material, Inorg. Chim. Acta 503 (2020) 119412, https://doi.org/10.1016/j.ica.2020.119412.
[35] A. Kumar, A. Sharma, Y. Chen, M.M. Jones, S.T. Vanyo, C. Li, M.B. Visser, S. D. Mahajan, R.K. Sharma, M.T. Swihart, Copper@ZIF-8 core-shell nanowires for reusable antimicrobial face masks, Adv. Funct. Mater. 31 (2021) 2008054, https://doi.org/10.1002/adfm.202008054.

[36] N. Nagarjun, A. Dhakshinamoorthy, A Cu-Doped ZIF-8 metal organic framework as a heterogeneous solid catalyst for aerobic oxidation of benzylic hydrocarbons, New J. Chem. 43 (2019) 18702–18712, https://doi.org/10.1039/C9NJ03698A.
[37] Y. Li, X. Peng, X. Li, H. Duan, S. Xie, L. Dong, F. Kang, Functional ultrathin separators proactively stabilizing zinc anodes for zinc-based energy storage, Adv. Mater. 35 (2023) 2300019, https://doi.org/10.1002/adma.202300019.
[38] T. Wang, J. Fu, M. Zheng, Z. Yu, Dynamic control strategy for the electrolyte flow rate of vanadium redox flow batteries, Appl. Energy 227 (2018) 613–623, https://doi.org/10.1016/j.apenergy.2017.07.065.
[39] G. Kresse, J. Furthmüller, Efficiency of ab-initio total energy calculations for metals and semiconductors using a plane-wave basis set, Comput. Mater. Sci. 6 (1996) 15–50, https://doi.org/10.1016/0927-0256(96)00008-0.
[40] G. Kresse, J. Furthmüller, Efficient iterative schemes for *ab initio* total-energy calculations using a plane-wave basis set, Phys. Rev. B 54 (1996) 11169–11186, https://doi.org/10.1103/PhysRevB.54.11169.
[41] P.E. Blöchl, Projector augmented-wave method, Phys. Rev. B 50 (1994) 17953–17979, https://doi.org/10.1103/PhysRevB.50.17953.
[42] V. Wang, N. Xu, J.C. Liu, G. Tang, W.T. Geng, VASPKIT: a user-friendly interface facilitating high-throughput computing and analysis using VASP code, Comput. Phys. Commun. 267 (2021) 108033, https://doi.org/10.1016/j.cpc.2021.108033.